

Uplink NOMA for Cellular-Connected UAV: Impact of UAV Trajectories and Altitude

Nilupuli Senadhira, *Student Member, IEEE*, Salman Durrani, *Senior Member, IEEE*, Xiangyun Zhou, *Senior Member, IEEE*, Nan Yang, *Senior Member, IEEE*, and Ming Ding, *Senior Member, IEEE*

Abstract

This paper considers an emerging cellular-connected unmanned aerial vehicle (UAV) architecture for surveillance or monitoring applications. We consider a scenario where a cellular-connected aerial user equipment (AUE) periodically transmits in uplink, with a given data rate requirement, while moving along a given trajectory. For efficient spectrum usage, we enable the concurrent uplink transmission of the AUE and a terrestrial user equipment (TUE) by employing power-domain aerial-terrestrial non-orthogonal multiple access (NOMA), while accounting for the AUE's known trajectory. To characterize the system performance, we develop an analytical framework to compute the rate coverage probability, i.e., the probability that the achievable data rate of both the AUE and TUE exceeds the respective target rates. We use our analytical results to numerically determine the minimum height that the AUE needs to fly, at each transmission point along a given trajectory, in order to satisfy a certain quality of service (QoS) constraint for various AUE target data rates and different built-up environments. Specifically, the results show that the minimum height of the AUE depends on its distance from the BS as the AUE moves along the given trajectory. Our results highlight the importance of modeling AUE trajectory in cellular-connected UAV systems.

Index Terms

Wireless communication, unmanned aerial vehicle (UAV), non-orthogonal multiple access (NOMA), trajectory, stochastic geometry.

N. Senadhira, S. Durrani, X. Zhou, and N. Yang are with the Research School of Electrical, Energy and Materials Engineering, College of Engineering and Computer Science, The Australian National University, Canberra, Australia (Emails: {nilupuli.senadhira, salman.durrani, xiangyun.zhou, nan.yang}@anu.edu.au). M. Ding is with Data61, CSIRO, Australia (Email: ming.ding@data61.csiro.au).

Part of this work has been submitted in IEEE ICC 2020 for possible conference publication [1].

I. INTRODUCTION

Due to their low cost, ease of deployment and mobility, unmanned aerial vehicles (UAVs) or drones are envisaged to find ever increasing use cases in civilian and commercial applications such as surveillance and monitoring, remote sensing, goods delivery, aerial photography and transporting human organs across a city [2]. Developing cellular support for UAVs has, therefore, been a hot topic of recent research [3]–[7]. Depending on whether UAVs are used as base stations to assist wireless communication of ground users, or as aerial users, there are two main paradigms for incorporating UAVs into cellular networks [3]: (i) UAV-assisted wireless communications and (ii) cellular-connected UAVs. UAV-assisted wireless communications, where UAVs act as aerial base stations (BSs), access points, relays, data aggregators, are regarded as a promising futuristic paradigm. However, before leaping forward with the deployment of UAV BSs, cellular-connected UAVs as user equipments (UEs) are being considered by standardization bodies as a priority for now [7]. For instance, the 3rd Generation Partnership Project (3GPP) is expected to consider cellular-connected UAVs in Release-17, which is expected to be finalized by September 2021 [2]. Hence, how to seamlessly and efficiently integrate aerial user equipments (AUEs) into existing cellular networks with terrestrial UEs becomes an important problem.

Trials by a number of leading industry vendors have demonstrated the feasibility of using existing cellular networks to support UAVs in the low-altitude airspace [8], [9]. In particular, it has been shown that terrestrial BSs with downtilted antennas provide adequate coverage via antenna side lobes for UAVs flying below 120 m [6]. While the antenna side lobes have reduced gain, this is offset by favorable line-of-sight (LoS) links. However, at higher altitudes, the gain from LoS links diminishes and the coverage becomes insufficient. In [10], the use of co-ordinated multi-point (CoMP) transmission was investigated for serving aerial users, which was shown to increase the coverage up to 200 m altitude. The results in [5], [8]–[10] assumed dedicated resources allocated to an aerial UE. However, this may not be efficient in future wireless networks as the resources dedicated to aerial users may be underutilized [5].

Recently, non-orthogonal multiple access (NOMA) has been proposed as a promising technology to address the resource scarcity issue in wireless communications [11]. The basic idea of NOMA is to serve multiple users in the same resource block, leading to more efficient resource utilization compared to conventional orthogonal multiple access [12], [13]. The use of NOMA in UAV-assisted wireless communication has been widely explored [14]–[18]. These studies focused on UAVs serving terrestrial users using NOMA in both microwave [14] and mmwave [15] bands,

resource allocation [16] or trajectory optimization problems [14], [17], [18]. *On the other hand, only a few studies have investigated the use of NOMA in cellular-connected UAV networks [19]–[21].* The energy efficiency of a NOMA scheme in a downlink mmwave cellular-connected UAV network was investigated and optimized in [21]. A beamforming strategy exploiting NOMA technique was proposed in [19] to allow an UAV to send its data to a selected subset of terrestrial BSs, which decode the UAV signal and then cancel it before decoding the messages of their served terrestrial users. By assuming the co-operative interference cancellation among the terrestrial BSs via backhaul links, a co-operative NOMA scheme for cellular-connected UAVs was proposed in [20]. However, the coexistence of terrestrial and aerial UEs was not considered in [21]. In addition, the UAV mobility was not considered in [19]–[21].

Mobility is an intrinsic characteristic of UAVs, which must be properly accounted for in the modeling and design of UAV systems. In UAV-assisted wireless networks, different approaches have been taken to model the mobility of aerial BSs. Studies adopting optimization techniques focused on optimal positioning [22], [23] or trajectory planning [24]–[26] problems and account for UAV mobility. Studies adopting stochastic geometry techniques typically assumed stationary UAVs and modeled them using Poisson or Binomial Point processes [27]–[31]. Recently, some progress has been made in mobility modeling of UAVs. Two trajectory processes for aerial BSs that provide the same uniform coverage behavior as the uniform Binomial Point Process were proposed in [32]. Inspired from the 3GPP UAV mobility model, which models UAV mobility in a straight line at a fixed height with a fixed speed, Random walk and Random waypoint models have been used to model the UAV movement in horizontal and/ or vertical directions [33], [34]. However, the system performance in [33], [34] is characterized from a time-average perspective, rather than the location of the UAV at a particular point along its trajectory. For cellular-connected UAVs, the prior relevant studies in [19]–[21] have considered stationary aerial users only. *To the best knowledge of the authors, the use of NOMA to efficiently serve both aerial and terrestrial users, while accounting for mobility of cellular-connected UAVs, has not been investigated in the literature to date.*

A. Paper Contributions

In this work, we consider a cellular-connected aerial UE (AUE) employed for surveillance or monitoring a cellular region. The AUE periodically transmits its data to the BS with a target data rate requirement. For efficient spectrum usage, we enable the concurrent uplink transmissions

by the AUE and a terrestrial UE (TUE) by employing power-domain aerial-terrestrial uplink NOMA. The main contributions of this work are as follows:

- We consider a successive interference cancellation (SIC) decoding strategy where the BS decodes the AUE first by treating the TUE as interference. If the AUE cannot be decoded then the BS tries to decode the TUE first and then the AUE. This decoding order leverages the fact that generally AUE link is stronger than the TUE one due to the favorable line-of-sight propagation. However, if the AUE is flying close to the cell edge and the TUE is located close to the BS, then the TUE link may be stronger than the AUE link.
- Using stochastic geometry, we develop a general analytical framework to compute the rate coverage probability, i.e., the probability that the achievable data rates of both the AUE and TUE exceeds the respective threshold target rates. The proposed framework explicitly incorporates the given trajectory of a cellular-connected AUE. Using the proposed framework, we determine the minimum height of the AUE for each transmission point along its given trajectory in order to meet a certain quality of service (QoS) in terms of the coverage probability for different built-up environments.
- Our results show that for a spiral trajectory, the minimum height increases as the AUE moves from the center to the cell edge. For low to moderate AUE target data rates, the target QoS is satisfied along the entire trajectory for suburban, urban and dense urban environments, and along the initial part of the trajectory for the urban high-rise environment. For the trajectory model adapted from the 3GPP recommendations, the minimum height of the AUE depends on its distance from the BS. The results highlight the importance of modeling the mobility related aspects in the design of NOMA-assisted cellular connected AUEs.

B. Notation and Paper Organization

The following notation is adopted in this paper. $\mathbb{P}(\cdot)$ and $\mathbb{E}[\cdot]$, denote the probability and expectation operator, respectively. $f_X(x)$ and $F_X(x)$ denote the probability density function (PDF) and cumulative distributive function (CDF) of a random variable X , respectively. $\lfloor \cdot \rfloor$ indicates the floor function.

The rest of the paper is organized as follows. Section II details the system model and the assumptions. Section III describes the proposed NOMA scheme which enables the simultaneous uplink transmissions of the AUE and the paired TUE. Section IV presents the analytical framework that is used to compute the rate coverage probabilities. Section V presents the results and

highlights the impact of the system parameters on the system performance. Finally, Section VI concludes the paper.

II. SYSTEM MODEL

We consider a single-cell wireless communication system with a terrestrial base station (BS), multiple stationary terrestrial user equipment (TUEs), and an aerial user equipment (AUE). The TUEs transmit in the uplink to the BS in a time division multiple access (TDMA) fashion, where each TUE in the cell is assigned a random orthogonal time slot to transmit its data to the BS. Hence, there is no intra-cell interference among the TUEs in the cell. The AUE is employed for surveillance or monitoring the region. Depending on the nature of the surveillance, the AUE has a target data rate requirement. It periodically transmits its data to the BS. For efficient spectrum usage, we assume that the AUE is not assigned a dedicated time slot for its uplink transmission. Hence, the AUE's uplink transmission interferes with the TUE transmitting at the same time. In this work, we propose to conduct uplink communication between the AUE and BS by pairing the transmissions of the AUE and a random TUE using non-orthogonal multiple access (NOMA). The TUE paired with the AUE is referred to as the *active* TUE. We assume that the active TUEs in the neighbouring cells are assigned orthogonal resource blocks (RBs) to mitigate terrestrial inter-cell interference [20]. Moreover, the AUE transmits at the same RB as the active TUE. Thus, in this work, we focus on the scenario with a single BS and a single AUE in a cell, without the presence of inter-cell interference.

A. Spatial Model

The single-cell is modeled as a disk region \mathcal{S} with a radius R . Without loss of generality, we adopt the three-dimensional (3D) cartesian coordinate system in this work. The BS is located at the center of the cell at a fixed height h_{BS} , i.e., at coordinates $(0, 0, h_{BS})$. In this work, we focus on the AUE pairing with a random TUE. Hence, an assumption on the number of TUEs is not required. We assume that the active TUE is randomly located in the disk region at coordinates $(x_T, y_T, 0)$ where $r_T = \sqrt{x_T^2 + y_T^2}$ is the horizontal distance between the BS and the active TUE.

B. AUE Trajectory and Mobility Model

The AUE trajectory and mobility model is illustrated in Fig. 1. We assume that the AUE flies along a given trajectory \mathcal{T} to cover the disk region, with a constant speed v_A at an altitude h_A

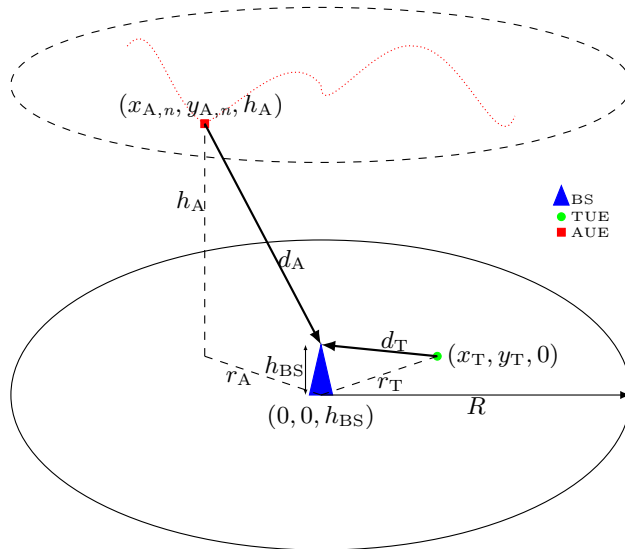


Fig. 1. Illustration of the three-dimensional system model. Blue triangle, red square, and green circle represent the BS, AUE, and TUE, respectively. AUE's arbitrary trajectory is denoted by the red dotted line.

above the ground¹. The AUE's uplink transmissions are periodic with time period T_A , resulting in N transmission points along the trajectory \mathcal{T} , i.e., $\mathcal{T} \triangleq \{\mathcal{T}[n]\}_{n=1}^N$ where n is the transmission point index. In \mathcal{T} , we define N as $N = \lfloor \frac{s(\mathcal{T}[N])}{v_A T_A} \rfloor$, where $s(\mathcal{T}[N])$ is the total path length of \mathcal{T} and $\lfloor \cdot \rfloor$ is the floor function. $\mathcal{T}[n] = (x_{A,n}, y_{A,n}, h_A)$ denotes the cartesian coordinates of the location of the AUE at the n th transmission point, where $r_{A,n} = \sqrt{x_{A,n}^2 + y_{A,n}^2}$ is the horizontal distance between the projection of the AUE on the ground and the BS.

C. Channel Model

Recently, progress has been made in the understanding of different types of channels in UAV communications [29], [35], [36]. The different channels can include, air-to-air channel model (between UAVs in the sky), air-to-ground/ ground-to-air channel model (between a UAV and an user on the ground) and cellular-to-air/ air-to-cellular channel model (between a UAV and an elevated terrestrial BS). Note that the distinction between air-to-ground and air-to-cellular lies in the non-negligible height of the terrestrial BS [29], [35], [36].

¹Note that the AUE is capable of varying its height along the course of the trajectory. In Sections V C-D we assume that the AUE flies at a constant height along the entire trajectory and, in Sections V E-F, we consider a case where the AUE can vary its height at each trajectory point to achieve a certain quality of service.

In our system model we have the following two types of links: (i) air-to-cellular (A2C) channel between the AUE and the terrestrial BS and (ii) terrestrial channel between the active TUE and BS.

The terrestrial channel is modeled as a combination of a large-scale path-loss attenuation, with path-loss exponent α_T , and small-scale Rayleigh fading component, with fading power gain H_T . Due to the path-loss, the transmit signal power of TUE decays at a rate $d_T^{-\alpha_T}$, where $d_T = \sqrt{r_T^2 + h_{BS}^2}$ is the 3D propagation distance between the TUE and the BS.

Following the state-of-the-art in [29], [35], [36], the air-to-cellular (A2C) channel is modeled as a combination of a probabilistic distance and height dependent large-scale path-loss and small-scale Nakagami- m fading, with fading power gain H_A . The path loss is determined according to whether the A2C channel is line-of-sight (LoS) or non-line-of-sight (NLoS) with probabilities of occurrence \mathbb{P}_{LoS} and $1 - \mathbb{P}_{LoS}$, respectively. In this work, we consider the International Telecommunication Union (ITU) model for determining the probability of LoS. The details are presented in Section V. The corresponding path-loss is given as

$$\zeta_A = \begin{cases} \eta_L d_A^{-\alpha_L}, & \text{if LoS} \\ \eta_N d_A^{-\alpha_N}, & \text{if NLoS,} \end{cases} \quad (1)$$

where $d_A = \sqrt{r_A^2 + (h_A - h_{BS})^2}$ is the 3D propagation distance between the BS and the AUE, η_ν , α_ν , $\nu \in \{L, N\}$ are the additional attenuation factors and path-loss exponents for LoS and NLoS channels. The fading parameters for the LoS and NLoS channels are denoted by m_L and m_N , respectively.

D. Received Signal

We assume that the TUE and AUE are equipped with single omnidirectional antennas. In order to serve both the active TUE and AUE simultaneously, the BS is equipped with a dual antenna array [30], i.e., BS can simultaneously beamform towards an active TUE and AUE, with associated antenna gains G_T and G_A , respectively².

The AUE transmits with a fixed transmit power P_A . For the active TUE, we use the truncated channel inversion power control [36], [37]. We assume that the BS has a receiver sensitivity

²The focus of this work is not on the complicated antenna modeling. Thus, we use the ideal antenna model for simplicity.

of ρ_{\min} . Therefore, the active TUE adjusts its transmit power such that average signal power received at the BS is equal to the cutoff threshold ρ_T , where $\rho_T > \rho_{\min}$. Hence,

$$P_T = \rho_T d_T^{\alpha_T}. \quad (2)$$

Based on the aforementioned system model, the received signal at the BS due to an AUE located at coordinates $(x_{A,n}, y_{A,n}, h_A)$ and an active TUE located at coordinates $(x_T, y_T, 0)$ is

$$\Psi_{BS} = \sqrt{P_T d_T^{-\alpha_T}} H_T G_T \Psi_T + \sqrt{P_A \zeta_A H_A G_A} \Psi_A + \mathbf{n}, \quad (3)$$

where \mathbf{n} is the additive white Gaussian noise with variance σ^2 , and Ψ_ϱ , $\varrho \in \{T, A\}$ denotes the signal transmitted by active TUE and AUE, respectively.

III. PROPOSED NOMA SCHEME

The simultaneous uplink transmissions of the AUE and the active TUE are facilitated by using power-domain aerial-terrestrial uplink NOMA with successive interference cancellation (SIC) at the BS. Power-domain NOMA utilizes the power domain for user multiplexing, allowing the active TUE and AUE to share a single time-frequency resource block [12], [13]. SIC allows the signals of each user to be decoded successively at the receiver end.

In the uplink terrestrial NOMA, the user with the strongest channel link quality is decoded first while treating the users with weaker link quality as interference. Then, the decoded signal is subtracted from the superimposed signal before decoding the users with weaker link quality. This process is continued until the user with the weakest link quality is decoded [12]. Due to analytical tractability, most studies in terrestrial uplink NOMA evaluate the channel link quality based on the average received power of each user, e.g., [38]. The channel link quality ranking assumes that the user closest to the BS has the strongest channel link quality and vice versa. Thus, the decoding order in this case is fixed and distance dependent. However, the fixed decoding order ignores the possibility where the closer user experiences severe small-scale fading and farther user experiences weaker small-scale fading. This possibility is accounted for in dynamic decoding order in terrestrial NOMA [39], [40], where the channel link quality is ranked based on the instantaneous received power of each user, which considers both large-scale path loss and small-scale fading of the terrestrial users.

In this work we consider a SIC decoding strategy with adaptive decoding order. Due to the strong LoS environment of the aerial link, we assume that the received signal power corresponding to the AUE is stronger than that of the active TUE for most of the time. Based on this

assumption, we assume that the AUE is decoded first at the BS³. However, if the AUE cannot be decoded, then the BS tries to decode the TUE, and then the AUE. This additional decoding step accounts for the case, where the received power corresponding to the active TUE is greater than that of the AUE when the AUE is flying closer to the cell edge and the active TUE is located closer to the BS. A detailed description of the decoding events and the aforementioned extra decoding step of the proposed aerial-terrestrial NOMA scheme is presented below.

The tree diagram of the decoding events in the proposed NOMA scheme is illustrated in Fig. 2 and explained as follows. The received signal at the BS is comprised of the superimposed Ψ_A and Ψ_T signals, where Ψ_A and Ψ_T denote the signals transmitted by the AUE and TUE, respectively. With SIC at the BS, Ψ_A is decoded first by treating Ψ_T as interference. If Ψ_A is decoded successfully, Ψ_T is decoded using SIC. Otherwise, BS tries to decode Ψ_T while treating Ψ_A as interference. In this work, we assume that, if Ψ_A is not decoded successfully, then error propagation occurs, i.e., BS treats the AUE's entire signal as interference when decoding Ψ_T . If Ψ_A is decoded successfully, the error propagation factor is 0, i.e., AUE's entire signal is subtracted from the superimposed signal [41]. If Ψ_T is decoded successfully at this stage, BS tries to decode the previously unsuccessful Ψ_A using SIC.

Each branch of the probability tree in Fig. 2 corresponds to a joint decoding event where either/ both/ none of the signals are decoded. Events corresponding to each branch are defined as follows.

- E_1 : Event that Ψ_A (i.e., AUE) is decoded in the first step and Ψ_T (i.e., TUE) is decoded in the second step.
- E_2 : Event that Ψ_A is decoded in the first step and Ψ_T is not decoded in the second step.
- E_3 : Event that Ψ_A is not decoded in the first step, Ψ_T is decoded in the second step, and Ψ_A is decoded in the third step.
- E_4 : Event that Ψ_A is not decoded in the first step, Ψ_T is decoded in the second step, and Ψ_A is not decoded in the third step.
- E_5 : Event that Ψ_A is not decoded in the first step and Ψ_T is not decoded in the second step.

³We can also consider another decoding order case where the signal transmitted by the TUE is decoded first. The working principle of this case would be similar to the case where the signal transmitted by the AUE is decoded first. However, due to the nature of the proposed NOMA scheme, the decoding order has no effect on the system performance in terms of the metrics defined in Section IV. Thus, in this work, we only focus on the case where the signal transmitted by the AUE is decoded first.

Remark 1: Due to the extra decoding step (corresponding to events E_3 and E_4), the tree diagram in this work is different from the tree diagrams in prior studies in terrestrial NOMA [38], [42]. In addition, we take the dependency of individual decoding steps into account rather than making the assumption that the decoding steps are independent as done in [38].

The probability corresponding to each event E_i is given by $P_i = \mathbb{P}(E_i)$, where $i = 1, 2, 3, 4$. These probabilities will be derived in Section IV to characterize the system performance under the proposed NOMA scheme.

IV. ANALYTICAL FRAMEWORK

In this section, we analyze the performance of the system using the rate coverage probability as the performance metric.

Definition 1: The rate coverage probability is the probability that the achievable data rate of a user exceeds the target data rate. It is defined as $\mathbb{P}(B \log_2(1 + \text{SINR}_\varrho) \geq \pi_\varrho)$, where $\varrho \in \{\text{T}, \text{A}\}$ denotes TUE and AUE, and B , SINR_ϱ and π_ϱ correspond to the bandwidth, signal-to-interference-plus-noise ratio and target data rate of the user, respectively.

For analytical simplicity, we re-express the rate coverage probability as

$$P_{\text{cov}} = \mathbb{P}[\text{SINR}_\varrho \geq \theta_\varrho], \quad (4)$$

which is the complementary cumulative distribution function (CCDF) of SINR, where $\theta_\varrho = 2^{\frac{\pi_\varrho}{B}} - 1$ is the target SINR threshold of the user. Note that we evaluate the rate coverage probability at each trajectory point of AUE, by averaging it over the location of the active TUE, and small-scale fading of AUE and TUE.

For each trajectory point, we evaluate the performance by computing three main rate coverage probabilities as defined below. The following probabilities correspond to linear combinations of probabilities of joint decoding events defined in Section III.

- P_{Tot} : Rate coverage probability of the event where both AUE and TUE are decoded successfully and is given by $P_{\text{Tot}} = P_1 + P_3$.
- P_{AUE} : Rate coverage probability of the event where AUE is decoded successfully and is given by $P_{\text{AUE}} = P_1 + P_2 + P_3$.
- P_{TUE} : Rate coverage probability of the event where TUE is decoded successfully and is given by $P_{\text{TUE}} = P_1 + P_3 + P_4$.

The rest of this section presents the lemmas and propositions used in the derivation of P_{Tot} , P_{AUE} and P_{TUE} . The relationship between the main results is illustrated in Fig. 3.

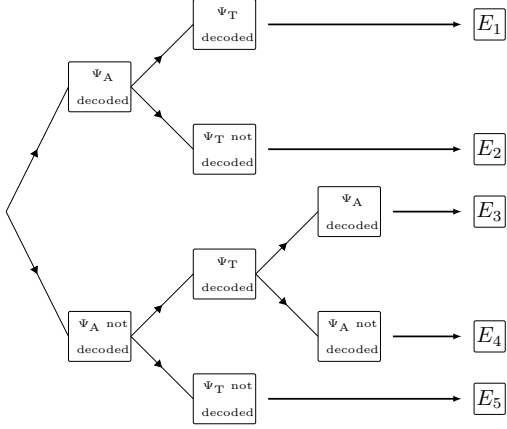


Fig. 2. Tree diagram of decoding events for proposed NOMA scheme.

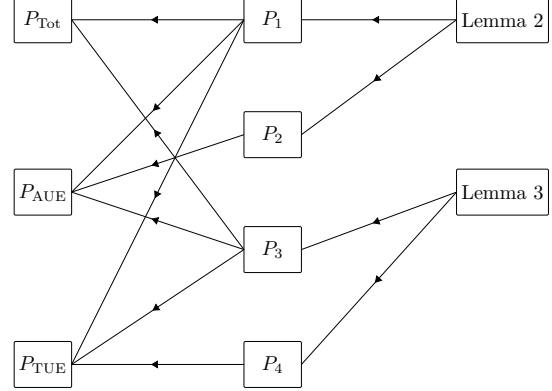


Fig. 3. Summary of the analytical framework metrics.

First we present three Lemmas, which help to derive the main results in this paper.

Lemma 1: The probability density function (PDF) of the 3D propagation distance d_T between BS and TUE is

$$f_{d_T}(z) = \frac{2z}{R^2}, \quad h_{BS} \leq z \leq \sqrt{R^2 + h_{BS}^2}. \quad (5)$$

Proof: See Appendix A. ■

Lemma 2: The cumulative distribution function (CDF) and PDF of the received power ψ_T corresponding to the active TUE, assuming TUE fading channel is Rayleigh fading, are

$$F_{\psi_T}(x) = 1 - \exp\left(\frac{-x}{\rho_T G_T}\right), \quad (6)$$

and

$$f_{\psi_T}(x) = \frac{1}{\rho_T G_T} \exp\left(\frac{-x}{\rho_T G_T}\right), \quad (7)$$

respectively, where $\psi_T = P_T d_T^{-\alpha_T} H_T G_T$.

Proof: See Appendix B. ■

Lemma 3: The CDF and PDF of the received power ψ_A corresponding to the AUE are

$$F_{\psi_A}(x) = 1 - \mathbb{P}_{\text{LoS}} \sum_{i=0}^{m_L-1} \frac{(\beta_L x)^i}{i!} \exp(-\beta_L x) - (1 - \mathbb{P}_{\text{LoS}}) \sum_{j=0}^{m_N-1} \frac{(\beta_N x)^j}{j!} \exp(-\beta_N x), \quad (8)$$

and

$$f_{\psi_A}(x) = \mathbb{P}_{\text{LoS}} \frac{\exp(-x\beta_L)\beta_L^{m_L} x^{m_L-1}}{\Gamma(m_L)} + (1 - \mathbb{P}_{\text{LoS}}) \frac{\exp(-x\beta_N)\beta_N^{m_N} x^{m_N-1}}{\Gamma(m_N)}, \quad (9)$$

respectively, where $\psi_A = P_A \zeta_A H_A G_A$, $\beta_L = \frac{m_L}{P_A \eta_L d_A^{-\alpha_L} G_A}$ and $\beta_N = \frac{m_N}{P_A \eta_N d_A^{-\alpha_N} G_A}$.

Proof: See Appendix B. ■

Next, we derive the rate coverage probabilities of the joint decoding events defined in Section III.

Proposition 1: The rate coverage probability that AUE is decoded in the first step and TUE is decoded in the second step is

$$P_1 = \frac{1}{\mu} \exp\left(\frac{\sigma^2}{\mu}\right) \left[\mathbb{P}_{\text{LoS}} \sum_{i=0}^{m_L-1} \frac{(\beta_L \theta_A)^i}{i!} \left(\beta_L \theta_A + \frac{1}{\mu}\right)^{-i-1} \Gamma\left(1+i, (1+\theta_T) \left(\beta_L \theta_A + \frac{1}{\mu}\right) \sigma^2\right) \right. \\ \left. + (1 - \mathbb{P}_{\text{LoS}}) \sum_{j=0}^{m_N-1} \frac{(\beta_N \theta_A)^j}{j!} \left(\beta_N \theta_A + \frac{1}{\mu}\right)^{-j-1} \Gamma\left(1+j, (1+\theta_T) \left(\beta_N \theta_A + \frac{1}{\mu}\right) \sigma^2\right) \right], \quad (10)$$

where $\mu = \rho_T G_T$.

Proof: The proof relies on stochastic geometry and is presented in Appendix C. ■

Proposition 2: The rate coverage probability that AUE is decoded in the first step and TUE is not decoded in the second step is

$$P_2 = \frac{1}{\mu} \exp\left(\frac{\sigma^2}{\mu}\right) \left[\mathbb{P}_{\text{LoS}} \sum_{i=0}^{m_L-1} \frac{(\beta_L \theta_A)^i}{i!} \left(\beta_L \theta_A + \frac{1}{\mu}\right)^{-i-1} \left[\Gamma\left(1+i, \left(\beta_L \theta_A + \frac{1}{\mu}\right) \sigma^2\right) \right. \right. \\ \left. \left. - \Gamma\left(1+i, (1+\theta_T) \left(\beta_L \theta_A + \frac{1}{\mu}\right) \sigma^2\right) \right] + (1 - \mathbb{P}_{\text{LoS}}) \sum_{j=0}^{m_N-1} \frac{(\beta_N \theta_A)^j}{j!} \left(\beta_N \theta_A + \frac{1}{\mu}\right)^{-j-1} \right. \\ \left. \times \left[\Gamma\left(1+j, \left(\beta_N \theta_A + \frac{1}{\mu}\right) \sigma^2\right) - \Gamma\left(1+j, (1+\theta_T) \left(\beta_N \theta_A + \frac{1}{\mu}\right) \sigma^2\right) \right] \right]. \quad (11)$$

Proof: The proof relies on stochastic geometry and is presented in Appendix C. ■

Proposition 3: The rate coverage probability that AUE is not decoded in the first step, TUE is decoded in the second step, and AUE is decoded in the third step is

$$P_3 = \begin{cases} \exp\left(\frac{-\theta_T \sigma^2}{\mu}\right) \left[\frac{\mathbb{P}_{\text{LoS}}}{\Gamma(m_L)} \beta_L^{m_L} \left(\beta_L + \frac{\theta_T}{\mu}\right)^{-m_L} \Gamma\left(m_L, \theta_A \left(\beta_L + \frac{\theta_T}{\mu}\right) \sigma^2\right) \right. \\ \left. + \frac{1-\mathbb{P}_{\text{LoS}}}{\Gamma(m_N)} \beta_N^{m_N} \left(\beta_N + \frac{\theta_T}{\mu}\right)^{-m_N} \Gamma\left(m_N, \theta_A \left(\beta_N + \frac{\theta_T}{\mu}\right) \sigma^2\right) \right], & \text{if } \theta_A \theta_T \geq 1 \\ \frac{\mathbb{P}_{\text{LoS}}}{\Gamma(m_L)} \exp\left(\frac{\sigma^2}{\mu}\right) \beta_L^{m_L} \left(\beta_L + \frac{1}{\theta_A \mu}\right)^{-m_L} \Gamma\left(m_L, \left(\beta_L \theta_A + \frac{1}{\mu}\right) \sigma^2\right) \\ \left. + \frac{1-\mathbb{P}_{\text{LoS}}}{\Gamma(m_N)} \exp\left(\frac{\sigma^2}{\mu}\right) \beta_N^{m_N} \left(\beta_N + \frac{1}{\theta_T \mu}\right)^{-m_N} \Gamma\left(m_N, \left(\beta_N \theta_A + \frac{1}{\mu}\right) \sigma^2\right) - \frac{1}{2} \frac{\theta_A \theta_T^2 \sigma^4 (1+\theta_A)^2}{(1-\theta_A \theta_T)}, \right. & \text{if } 0 \leq \theta_A \theta_T < 1. \end{cases} \quad (12)$$

Proof: The rate coverage probability P_3 can be expressed as

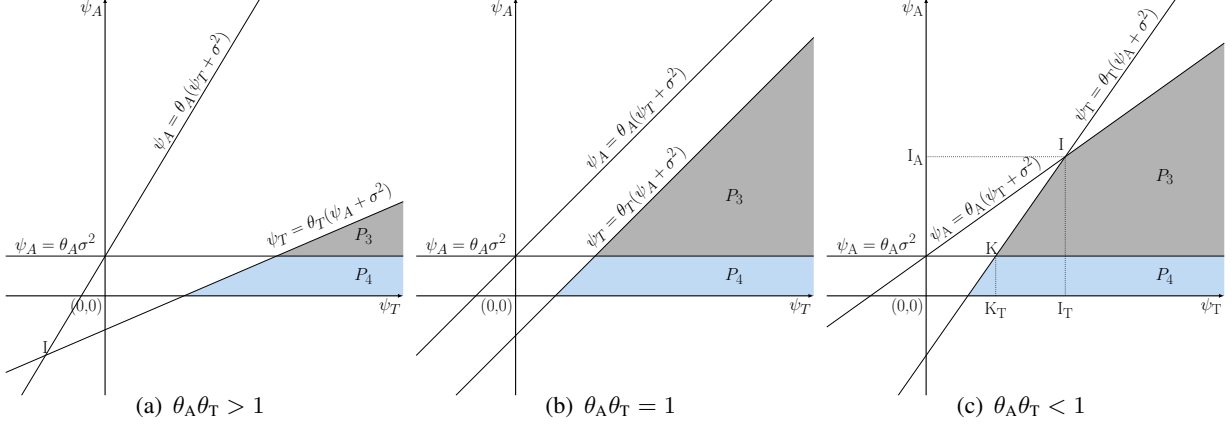


Fig. 4. Integral regions of P_3 and P_4 , when $\theta_A \theta_T > 1$, $\theta_A \theta_T = 1$, and $\theta_A \theta_T < 1$, respectively, for proof of Propositions 3 and 4.

$$\begin{aligned}
 P_3 &= \mathbb{P}_{\psi_A, \psi_T} \left(\frac{\psi_A}{\sigma^2} \geq \theta_A, \frac{\psi_T}{\psi_A + \sigma^2} \geq \theta_T, \frac{\psi_A}{\psi_T + \sigma^2} < \theta_A \right) \\
 &= \mathbb{P}_{\psi_A, \psi_T} \left(\psi_A \geq \theta_A \sigma^2, \psi_T \geq \theta_T (\psi_A + \sigma^2), \psi_A < \theta_A (\psi_T + \sigma^2) \right). \quad (13a)
 \end{aligned}$$

The inequalities in (13a) are plotted in Fig. 4. P_3 is derived by calculating the area covered by all three curves. The point of intersection of $\psi_A = \theta_A (\psi_T + \sigma^2)$ and $\psi_T = \theta_T (\psi_A + \sigma^2)$ is given by $I = \left(\frac{\theta_T \sigma^2 (1 + \theta_A)}{1 - \theta_A \theta_T}, \frac{\theta_A \sigma^2 (1 + \theta_T)}{1 - \theta_A \theta_T} \right)$. Depending on the value of $\theta_A \theta_T$, the point of intersection, I can be located in different quadrants or non-existent (in the case of $\theta_A \theta_T = 1$). Thus, P_3 can have different values in these cases.

We first present the proof of P_3 when $\theta_A \theta_T \geq 1$.

$$P_3 = \mathbb{P}_{\psi_A, \psi_T} (\psi_T \geq \theta_T (\psi_A + \sigma^2), \psi_A \geq \theta_A \sigma^2) \quad (14a)$$

$$\begin{aligned}
 &= \mathbb{E}_{\psi_A} [\mathbb{P}_{\psi_T} (\psi_T \geq \theta_T (a + \sigma^2), a \geq \theta_A \sigma^2)] \\
 &= \int_{\theta_A \sigma^2}^{\infty} \mathbb{P}_{\psi_T} (\psi_T \geq \theta_T (a + \sigma^2)) f_{\psi_A}(a) da \quad (14b)
 \end{aligned}$$

$$\begin{aligned}
 &= \int_{\theta_A \sigma^2}^{\infty} \mathbb{P}_{H_T, d_T} \left(H_T \geq \frac{\psi_T (a + \sigma^2)}{P_T d_T^{-\alpha_T} G_T} \right) f_{\psi_A}(a) da \\
 &= \int_{\theta_A \sigma^2}^{\infty} \mathbb{E}_{d_T} \left[\exp \left(-\frac{\theta_T (a + \sigma^2)}{P_T d_T^{-\alpha_T} G_T} \right) \right] f_{\psi_A}(a) da \quad (14c)
 \end{aligned}$$

$$= \int_{\theta_A \sigma^2}^{\infty} \left[\int_{h_{BS}}^{\sqrt{h_{BS}^2 + R^2}} \exp \left(-\frac{\theta_T (a + \sigma^2)}{\rho_T z^{\alpha_T} z^{-\alpha_T} G_T} \right) \left(\frac{2z}{R^2} \right) dz \right] f_{\psi_A}(a) da$$

$$= \int_{\theta_A \sigma^2}^{\infty} \exp\left(\frac{-\theta_T(a + \sigma^2)}{\rho_T G_T}\right) \left[\mathbb{P}_{\text{LoS}} \frac{\exp(-a\beta_L)\beta_L^{m_L} a^{m_L-1}}{\Gamma(m_L)} + (1 - \mathbb{P}_{\text{LoS}}) \frac{\exp(-a\beta_N)\beta_N^{m_N} a^{m_N-1}}{\Gamma(m_N)} \right] da, \quad (14d)$$

where (14a) is the simplified expression for the area of P_3 based on Fig. 4(a) and 4(b). (14c) comes from the fact that H_T follows an exponential distribution. Integration of (14d) with respect to a and substitution of $\mu = \rho_T G_T$ into (14d) yield (12) for the case $\theta_A \theta_T \geq 1$.

The proof of P_3 for the case $\theta_A \theta_T < 1$ is presented as follows. Let $I = (I_T, I_A)$, where I_T denotes the x-coordinate and I_A denotes the y-coordinate of point I, and, $K_T = \theta_T \sigma^2 (\theta_A + 1)$ is the x-coordinate of point K as illustrated in Fig. 4(c). Let $P_{3,Q}$ be the triangular area enclosed by the curves, $\psi_T = \theta_T(\psi_A + \sigma^2)$, $\psi_A = \theta_A \sigma^2$ and $\psi_T = I_T$. Let $P_{3,R}$ be the quadrilateral area enclosed by the curves, $\psi_A = \theta_A(\psi_T + \sigma^2)$, $\psi_A = \theta_A \sigma^2$ and $\psi_T = I_T$. Thus, we can write $P_3 = P_{3,Q} + P_{3,R}$. The derivations of $P_{3,Q}$ and $P_{3,R}$ are presented below.

$$P_{3,Q} = \frac{1}{2}(I_T - K_T)(I_A - \theta_A \sigma^2) = \frac{1}{2} \frac{\theta_A \theta_T^2 \sigma^2 (1 + \theta_A)}{(1 - \theta_A \theta_T)} \frac{\theta_A \theta_T \sigma^2 (1 + \theta_A)}{(1 - \theta_A \theta_T)} \quad (15a)$$

$$= \frac{1}{2} \frac{\theta_A^2 \theta_T^3 \sigma^4 (1 + \theta_A)^2}{(1 - \theta_A \theta_T)^2}, \quad (15b)$$

where (15a) is the area of a triangle.

$$P_{3,R} = \mathbb{P}_{\psi_A, \psi_T} (\psi_A < \theta_A(\psi_T + \sigma^2), \psi_A \geq \theta_A \sigma^2) - \frac{1}{2} I_T (I_A - \theta_A \sigma^2) \quad (16a)$$

$$\begin{aligned} &= \mathbb{E}_{\psi_A} \left[\mathbb{P}_{\psi_T} \left(\psi_T > \frac{a}{\theta_A} - \sigma^2, a \geq \theta_A \sigma^2 \right) \right] - \frac{1}{2} \frac{\theta_A \theta_T^2 \sigma^4 (1 + \theta_A)^2}{(1 - \theta_A \theta_T)^2} \\ &= \int_{\theta_A \sigma^2}^{\infty} \mathbb{P}_{\psi_T} \left(\psi_T > \frac{a}{\theta_A} - \sigma^2 \right) f_{\psi_A}(a) da - \frac{1}{2} \frac{\theta_A \theta_T^2 \sigma^4 (1 + \theta_A)^2}{(1 - \theta_A \theta_T)^2} \\ &= \int_{\theta_A \sigma^2}^{\infty} \exp\left(-\frac{(\frac{a}{\theta_A} - \sigma^2)}{\rho_T G_T}\right) f_{\psi_A}(a) da - \frac{1}{2} \frac{\theta_A \theta_T^2 \sigma^4 (1 + \theta_A)^2}{(1 - \theta_A \theta_T)^2}, \end{aligned} \quad (16b)$$

where (16a) is the difference between the triangular area enclosed by $\psi_A = \theta_A(\psi_T + \sigma^2)$ and $\psi_A = \theta_A \sigma^2$, and the triangular area enclosed by $\psi_A = \theta_A(\psi_T + \sigma^2)$, $\psi_A = \theta_A \sigma^2$ and $\psi_T = I_T$. Evaluating and simplifying (16b), we obtain (12). ■

Proposition 4: The rate coverage probability that AUE is not decoded in the first step, TUE is decoded in the second step, and AUE is not decoded in the third step is

$$\begin{aligned} P_4 &= \exp\left(\frac{-\theta_T \sigma^2}{\mu}\right) \left[\frac{\mathbb{P}_{\text{LoS}}}{\Gamma(m_L)} \beta_L^{m_L} \left(\beta_L + \frac{\theta_T}{\mu}\right)^{-m_L} \left[\Gamma(m_L) - \Gamma\left(m_L, \theta_A \left(\beta_L + \frac{\theta_T}{\mu}\right) \sigma^2\right) \right] \right. \\ &\quad \left. + \frac{1 - \mathbb{P}_{\text{LoS}}}{\Gamma(m_N)} \beta_N^{m_N} \left(\beta_N + \frac{\theta_T}{\mu}\right)^{-m_N} \left[\Gamma(m_N) - \Gamma\left(m_N, \theta_A \left(\beta_N + \frac{\theta_T}{\mu}\right) \sigma^2\right) \right] \right]. \end{aligned} \quad (17)$$

Proof: The rate coverage probability P_4 can be expressed as

$$\begin{aligned} P_4 &= \mathbb{P}_{\psi_A, \psi_T} \left(\frac{\psi_A}{\sigma^2} < \theta_A, \frac{\psi_T}{\psi_A + \sigma^2} \geq \theta_T, \frac{\psi_A}{\psi_T + \sigma^2} < \theta_A \right) \\ &= \mathbb{P}_{\psi_A, \psi_T} (\psi_A < \theta_A \sigma^2, \psi_T \geq \theta_T (\psi_A + \sigma^2), \psi_A < \theta_A (\psi_T + \sigma^2)) \end{aligned} \quad (18a)$$

$$= \mathbb{P}_{\psi_A, \psi_T} (\psi_A < \theta_A \sigma^2, \psi_T \geq \theta_T (\psi_A + \sigma^2)) = \mathbb{E}_{\psi_A} [\mathbb{P}_{\psi_T} (a < \theta_A \sigma^2, \psi_T \geq \theta_T (a + \sigma^2))] \quad (18b)$$

$$\begin{aligned} &= \int_0^{\theta_A \sigma^2} \mathbb{P}_{\psi_T} (\psi_T \geq \theta_T (a + \sigma^2)) f_{\psi_A}(a) da \\ &= \int_0^{\theta_A \sigma^2} \exp \left(-\frac{\theta_T (a + \sigma^2)}{\rho_T G_T} \right) f_{\psi_A}(a) da. \end{aligned} \quad (18c)$$

The inequalities in (18a) are plotted in Fig. 4. Note that the areas enclosed by the relevant curves do not vary with the value of $\theta_A \theta_T$. (18b) is the simplified expression for the quadrilateral area of P_4 . In (18c), the evaluation of $\mathbb{P}_{\psi_T} (\psi_T \geq \theta_T (a + \sigma^2))$ is similar to that in (14b). By integrating (18c) with respect to a , we obtain (17). ■

The final rate coverage probabilities P_{Tot} , P_{AUE} and P_{TUE} can be computed after evaluating P_1 , P_2 , P_3 and P_4 , as summarized in Fig. 3.

V. NUMERICAL RESULTS

In this section, we investigate the performance of the proposed NOMA scheme with respect to the AUE SINR threshold, TUE SINR threshold and AUE altitude. The accuracy of the derived analytical expressions is validated by comparing them with simulation results. The parameter values used for the results are given in Table I. The chosen values are consistent with other relevant works in the literature [6], [36], [43]. We assume a bandwidth of 10 MHz and consider AUE target SINR thresholds $\{0, 10, 20, 30, 40\}$ dB, corresponding to AUE target rates $\{10, 34.6, 66.6, 99.7, 134.6\}$ Mbps. We consider a target rate of 10 Mbps (corresponding to a target SINR threshold of 0 dB) for the TUE, unless stated otherwise.

A. Probabilistic LoS model

We adopt the probabilistic LoS model suggested in ITU recommendation report [44] by considering AUE as the transmitter and the terrestrial BS as the receiver. Thus, the probability of LoS between the AUE and the terrestrial BS is [45]

$$\mathbb{P}_{\text{LoS}} = \prod_{n_{\text{ITU}}=0}^{m_{\text{ITU}}} \left[1 - \exp \left(-\frac{\left[h_A - \frac{(n_{\text{ITU}} + \frac{1}{2})(h_A - h_{\text{BS}})}{m_{\text{ITU}} + 1} \right]^2}{2\delta_{\text{ITU}}} \right) \right], \quad (19)$$

TABLE I
PARAMETER VALUES FOR NUMERICAL AND SIMULATION RESULTS.

Parameter	Symbol	Value	Parameter	Symbol	Value
Cell radius	R	500 m	Number of rounds	m	3
Height of BS	h_{BS}	30 m	Time period for AUE's transmission	T_A	30 s
Noise power	σ^2	-100 dBm	AUE's transmit power	P_A	0.1 W
TUE			AUE's antenna gain	G_A	1
TUE's cutoff threshold	ρ_T	-75 dBm	Pathloss exponent for LoS link	α_L	2.2
TUE's antenna gain	G_T	1	Pathloss exponent for NLoS link	α_N	3.5
Pathloss exponent of terrestrial link	α_T	3.5	Attenuation for LoS link	η_L	0 dB
AUE			Attenuation for NLoS link	η_N	13 dB
AUE's speed	v_A	15 m/s	Fading parameter for LoS link	m_L	5
AUE's altitude	h_A	25 m, 120 m	Fading parameter for NLoS link	m_N	1

where $m_{ITU} = \left\lfloor \left(\frac{r_A \sqrt{\alpha_{ITU} \beta_{ITU}}}{1000} - 1 \right) \right\rfloor$ and $\lfloor \cdot \rfloor$ is the floor function. α_{ITU} , β_{ITU} and δ_{ITU} correspond to the environment-related parameters that can be used to describe the built-up area. α_{ITU} and β_{ITU} correspond to the ratio of land area covered by buildings to total land area, and the average number of buildings per unit area, respectively. δ_{ITU} is the parameter for the Rayleigh distribution that determines the building heights. The values of these parameters for suburban, urban, dense urban and urban high-rise environments are given in Table I in Page 2 in [46].

Fig. 5 illustrates the probabilistic LoS behavior for two different AUE altitudes. Fig. 5(a) demonstrates the variation of LoS probability with the horizontal distance of AUE from the BS, whereas Fig. 5(b) shows the variation of the LoS probability with angle of elevation between the AUE and BS. Note that both plots exhibit step-wise discrete behavior due to the blockage caused by buildings in the urban built-up area. This behavior becomes smooth and continuous at very high AUE altitudes. However, in this work, we consider a practical AUE altitude range of 25 – 300 m.

B. AUE Trajectory Model

For the purpose of generating the results, we model the trajectory of AUE using an Archimedes' spiral. The Archimedes' spiral has a special property that any ray from the origin intersects successive turnings of the spiral in points with a constant separation distance. Hence, it is a suitable trajectory for monitoring or surveillance in a disk region. *Note that the proposed*

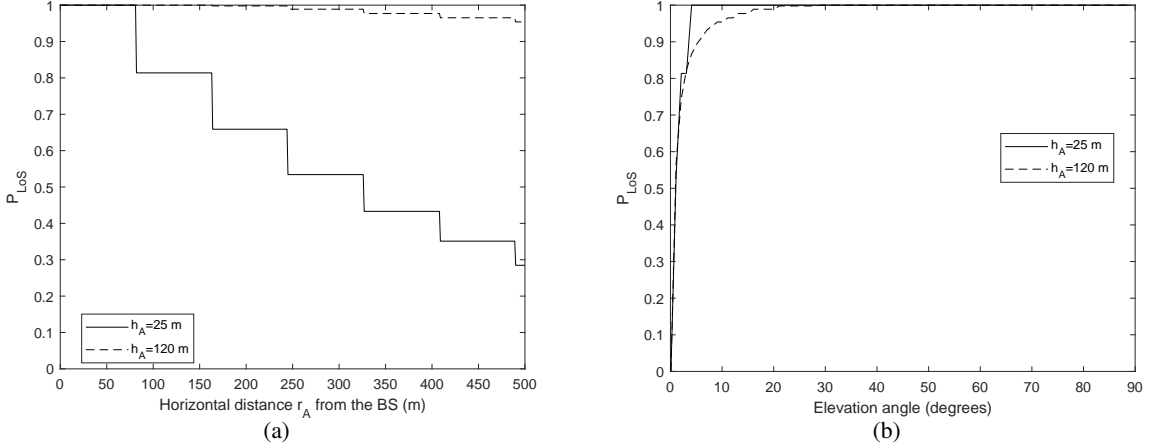


Fig. 5. Probability of line-of-sight, \mathbb{P}_{LoS} versus (a) horizontal distance from the BS r_A (m), and (b) elevation angle between the AUE and BS. The adopted values for the environmental parameters corresponding to the urban built-up area are, $\alpha_{\text{ITU}} = 0.3$, $\beta_{\text{ITU}} = 500$ and $\delta_{\text{ITU}} = 15$.

framework in this paper is valid for any trajectory model. In Sections V C-E we consider the Archimedes' spiral trajectory and in Section V-F we consider the 3GPP trajectory model.

The AUE starts its spiral trajectory at the center of the cell at a height h_A . The trajectory of the AUE can be described by a spiral with equation $r_A = \frac{R}{2\pi m} \phi_A$, where m is the number of rounds and ϕ_A is the orientation of AUE in the azimuth plane, measured with respect to the +x-axis. The equation for r_A is derived based on the assumption that the spiral starts at the center of the cell and reaches the cell edge at $\phi_{\text{AEdge}} = 2\pi m$ which is the maximum angle in the azimuth plane for a given number of rounds. Hence, the expressions for N and $r_{A,n}$ for the Archimedes' spiral are given as follows:

The number of transmission points along the AUE trajectory defined by the Archimedes' spiral is given by

$$N = \left\lfloor \frac{R \left(2\pi m \sqrt{1 + (2\pi m)^2} + \sinh^{-1}(2\pi m) \right)}{4\pi m v_A T_A} \right\rfloor. \quad (20)$$

The horizontal distance $r_{A,n}$ between the AUE and BS at the n th transmission point is

$$r_{A,n} = R \sqrt{\frac{n}{N}}, \quad (21)$$

where $n = 1, \dots, N$.

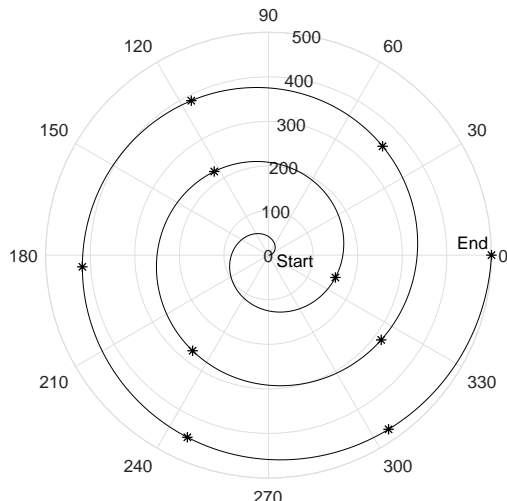


Fig. 6. Archimedes' spiral trajectory with $m = 3$ and $R = 500$ m. AUE's transmission points are denoted by asterisk ($v_A = 15$ m/s, $T_A = 30$ s).

Fig. 6 demonstrates the Archimedes' trajectory for the case where the AUE travels three complete rounds to reach the cell edge. The AUE performs uplink transmission at 10 points along the trajectory, and the final transmission point lies at the cell edge.

C. Model Validation

Fig. 7 presents the total rate coverage probability P_{Tot} for an aerial-terrestrial network where the AUE flies according to an Archimedes' trajectory at a fixed height h_A along the entire trajectory. The model validation results are presented only for P_{Tot} , since P_{AUE} and P_{TUE} exhibit similar trends as that for P_{Tot} . We present the results when $\theta_T = 0$ dB and AUE flies at altitudes 25 m and 120 m. We see that the analytical results match well with the simulation results. This validates the accuracy of the analytical framework in Section IV. The figure shows that P_{Tot} generally decreases when AUE's SINR threshold (corresponds to AUE's target data rate) increases and when the horizontal distance between the AUE and the BS increases, for both altitudes. For the ITU probabilistic LoS model, the performance is better at 120 m compared to that at 25 m, and the rate coverage probabilities decrease when the AUE flies away from the BS. This is due to the fact that in the ITU probabilistic LoS model, the probability of LoS is higher at 120 m compared to that in 25 m and, the probability of LoS decreases with the increase in r_A (see Fig. 5(a)).

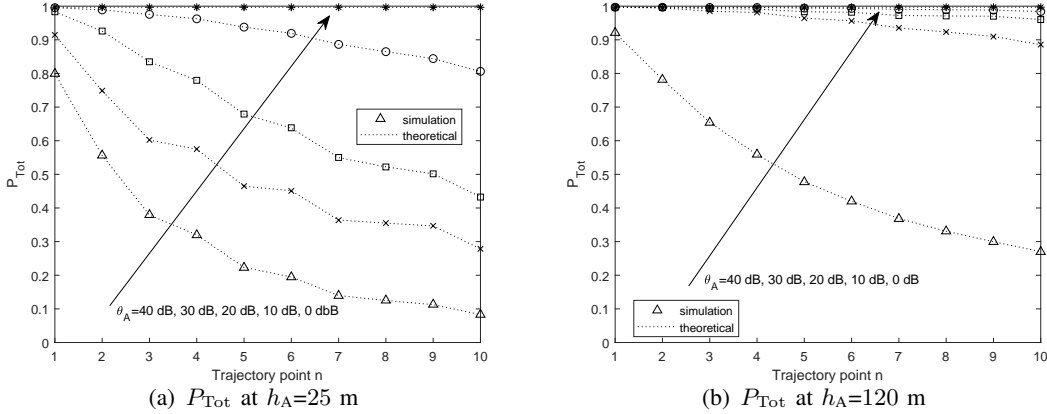


Fig. 7. Rate coverage probabilities of the events where both AUE and TUE are decoded (P_{Tot}) for (a) $h_A = 25$ m and (b) $h_A = 120$ m. The simulation values and the theoretical values are represented by markers and dotted lines, respectively.

In the next two subsections, we only present the numerical results using the proposed analytical framework due to the accuracy of our analytical results.

D. Impact of SINR Thresholds of TUE and AUE

Fig. 8 shows the impact of θ_T (equivalently, the target data rate of TUE), on rate coverage probabilities P_{Tot} , P_{AUE} and P_{TUE} for different θ_A values along the spiral trajectory. The results are presented for two different AUE heights (25 m and 120 m). $n = 1$ corresponds to the first transmission point and $n = 10$ corresponds to the last transmission point when the AUE reaches the cell edge (see transmission points marked in Fig. 6).

Fig. 8 shows that depending upon the SINR threshold of TUE and SINR threshold of AUE, P_{Tot} can be dominated by either decoding of TUE or AUE. For both heights, when $\theta_T = 0$ dB (see Fig. 8(a) and 8(c)) we can see that P_{Tot} , P_{AUE} and P_{TUE} have similar rate coverage probability values for lower θ_A values (0 – 20 dB). However, this trend changes at $\theta_A = 30$ dB and 40 dB. When AUE is flying at 25 m (see Fig. 8(a)) and is closer to the cell edge, P_{TUE} is slightly higher than P_{Tot} and P_{AUE} at $\theta_A = 30, 40$ dB. This is caused by the high path loss and poor LoS aerial links in proximity to the cell edge. *In this case, P_{Tot} is dominated by the decoding of AUE.* However, this behavior becomes less prominent at higher AUE heights (see Fig. 8(c)). This is because at higher AUE heights, the AUE is almost always guaranteed to be successfully decoded due to the strong LoS aerial links.

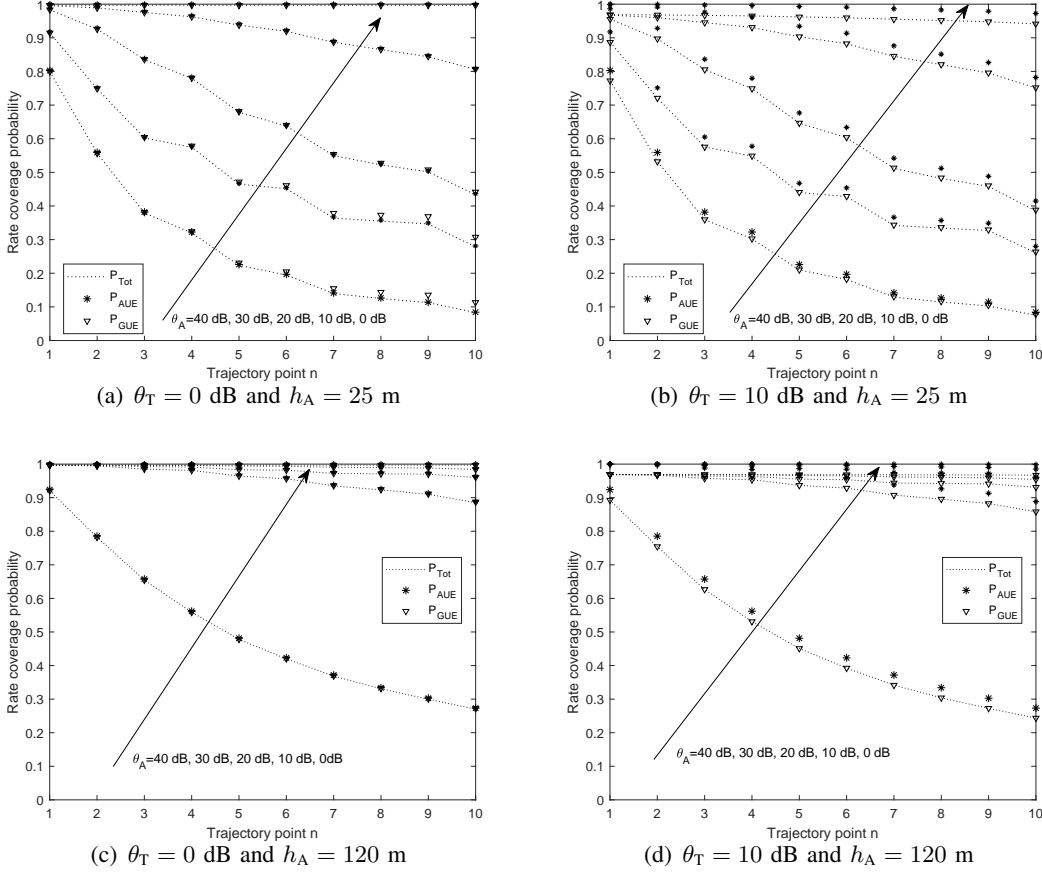


Fig. 8. Rate coverage probabilities P_{Tot} , P_{AUE} and P_{TUE} vs. trajectory point n for different $\theta_A = 0, 10, 20, 30, 40$ dB and, (a) $\theta_T = 0$ dB and $h_A = 25$ m, (b) $\theta_T = 10$ dB and $h_A = 25$ m, (c) $\theta_T = 0$ dB and $h_A = 120$ m and (d) $\theta_T = 10$ dB and $h_A = 120$ m. P_{Tot} , P_{AUE} and P_{TUE} are denoted by solid line, asterisk and circle, respectively.

Fig. 8(b) and 8(d) compare the rate coverage probabilities at $\theta_T = 10$ dB for $h_A = 25$ and 120 m. At both heights, P_{Tot} is similar to P_{TUE} for low to moderate θ_A values (0, 10, 20, 30 dB). This implies that P_{Tot} is dominated by the decoding of TUE at higher θ_T for low to moderate θ_A . In Fig. 8(b), we can see that this effect becomes insignificant when θ_A is higher and AUE is flying at a relatively low height. It is important to note that this behavior in Fig. 8(b) is consistent throughout the trajectory at a higher θ_T , unlike in Fig. 8(a), where the trend changes as the AUE moves from cell center to cell edge. At 120 m, due to the strong LoS aerial links, P_{Tot} is dominated by the decoding of TUE for all considered θ_A values throughout the trajectory at higher θ_T values (see Fig. 8(d)). Note that the trends of P_{AUE} and P_{TUE} are similar to that of P_{Tot} for each of the cases presented in Fig. 8. Thus, for the rest of the results section, we only present the corresponding results for P_{Tot} .

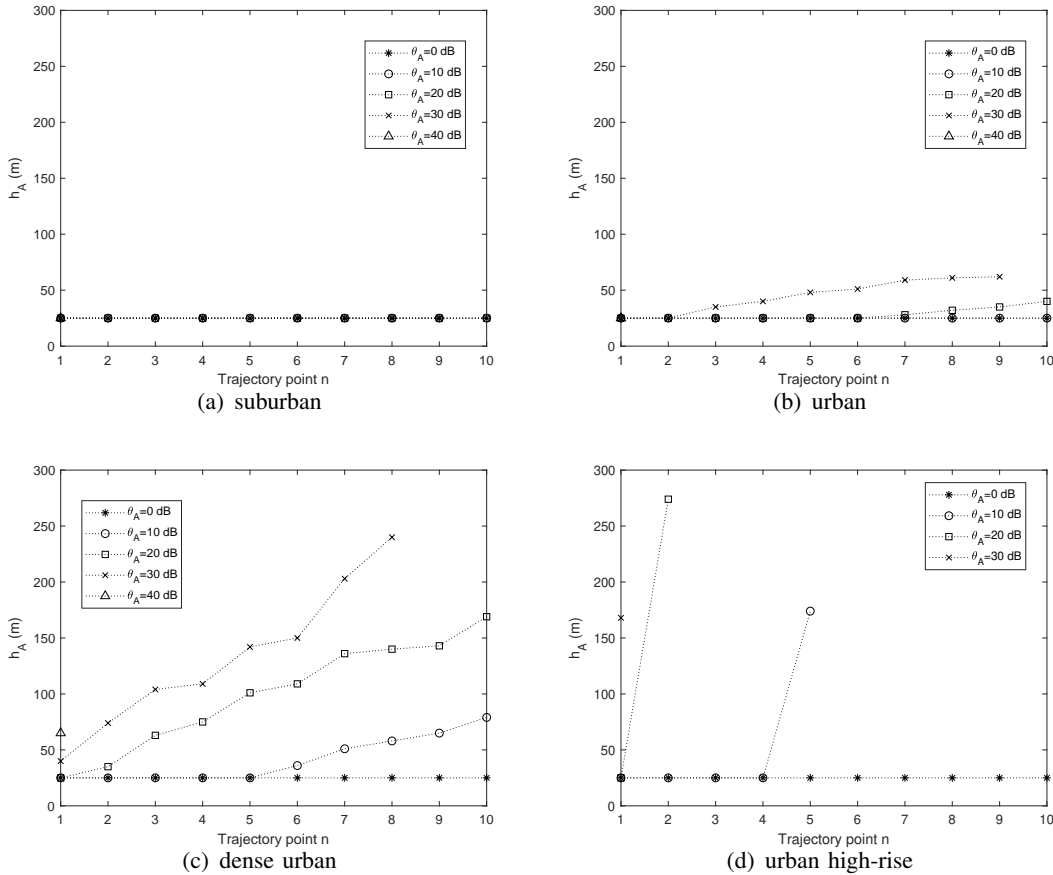


Fig. 9. Minimum height of AUE to achieve a total rate coverage probability of 0.9 vs. the trajectory point for (a) suburban, (b) urban, (c) dense urban and (d) urban high-rise environments.

E. Impact of AUE Altitude and Built-Up Environments

Previously, we assumed that the AUE flies at a constant height in a spiral trajectory. Now we consider the case where the AUE still follows the spiral trajectory, but it can ascend or descend at each trajectory point to achieve a certain quality of service (QoS).

We define the QoS as the probability where both AUE and TUE are decoded, which is equivalent to P_{Tot} . Current regulations in most countries do not permit AUEs to fly higher than a certain height [5], [6]. Hence, in this section, we focus on the minimum height of AUE at each trajectory point, to achieve a QoS of 90% (corresponds to $P_{\text{Tot}} = 0.9$) for different built-up environments.

Fig. 9 plots P_{Tot} versus the minimum height to meet QoS constraint for different environments. From Fig. 9(a) for the suburban environment, we can see that due to the lower building density

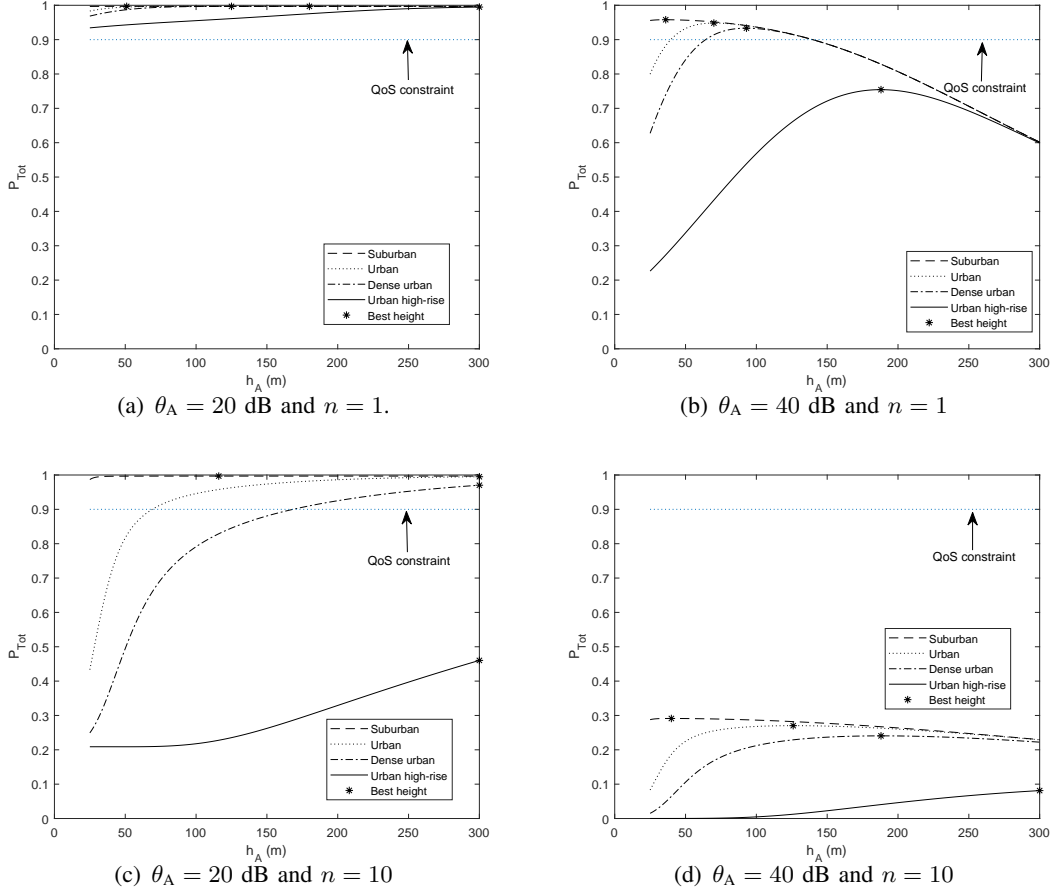


Fig. 10. Total rate coverage probability vs. AUE height h_A for different environments for (a) $\theta_A = 20$ dB and $n = 1$, (b) $\theta_A = 40$ dB and $n = 1$, (c) $\theta_A = 20$ dB and $n = 10$ and (d) $\theta_A = 40$ dB and $n = 10$. The best AUE height where P_{Tot} is maximum is indicated by markers. Dotted line correspond to a P_{Tot} threshold of 0.9.

and shorter building height, a QoS of 90% can be achieved by the AUE even if it is flying at a very low height of 25 m. However, for the rest of the environments (see Fig. 9(b), 9(c) and 9(d)), the AUE needs to ascend when AUE flying towards the cell edge, in order to meet the QoS requirement. Moreover, this minimum height increases when the environmental parameters become severer. For an instance, for urban high-rise environment (see Fig. 9(d)), where there is a high density of taller buildings, a target QoS of 90% cannot be achieved for higher θ_A and r_A values even if the AUE is flying at a height of 300 m. Moreover, the target QoS at $\theta_A = 40$ dB can only be satisfied at the first trajectory point (closer to the BS) for urban and dense urban built-up environments, and can not be satisfied at all for urban high-rise environment.

Since the first ($n = 1$) and last ($n = 10$) trajectory points represent the best and worst cases

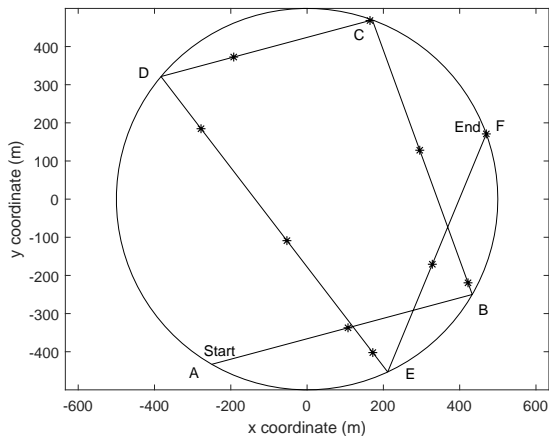


Fig. 11. 3GPP-inspired trajectory model.

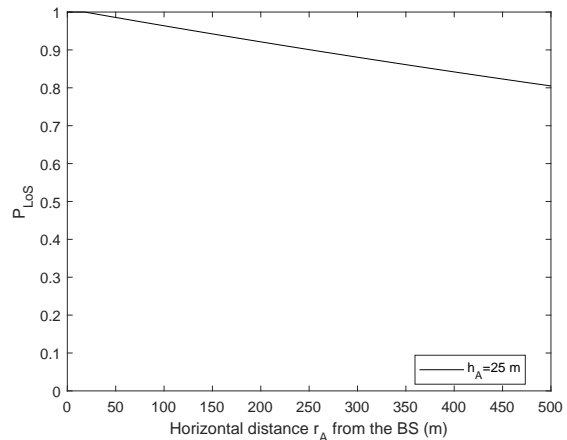


Fig. 12. 3GPP probabilistic LoS model.

for the spiral trajectory, we also look at the variation of P_{Tot} with respect to the height of AUE at these trajectory points. We compare the P_{Tot} for two different TUE SINR threshold values at $n = 1$ and $n = 10$ (see Fig. 10). At $\theta_A = 20$ dB (see Fig. 10(a) and 10(c)), P_{Tot} increases as the AUE height increases at both trajectory points. However, at $\theta_A = 40$ dB (see Fig. 10(b) and 10(d)), there is a best height where the P_{Tot} is maximized. This trend is prominent when the AUE is closer to the BS (see Fig. 10(b)), and becomes less significant when AUE is closer to the cell boundary (see Fig. 10(d)). Moreover, the best height increases as the environmental conditions become severer for both trajectory points. Note that for $\theta_A = 20$ dB, the best height satisfies the QoS constraint of $P_{\text{Tot}} = 0.9$, except for urban high-rise at $n = 10$. For $\theta_A = 40$ dB, the best height satisfies the QoS constraint only for some environments at cell center ($n = 1$) and none of the environments at cell edge ($n = 10$).

Next, we apply the proposed NOMA scheme to an AUE trajectory inspired by the 3GPP mobility model in [43].

F. 3GPP Probabilistic LoS and Mobility Models

We adopt the mobility model and probabilistic LoS model proposed in [43] for this evaluation. In 3GPP probabilistic LoS model, the probability of LoS between the AUE and the terrestrial BS, in the urban environment where the BS antennas are positioned above the rooftop levels of

buildings is [43]

$$\mathbb{P}_{LoS} = \begin{cases} \frac{d_1}{r_A} + \exp\left(\frac{-r_A}{p_1}\right) \left(1 - \frac{d_1}{r_A}\right), & \text{if } r_A > d_1, 22.5 < h_A \leq 100 \\ 1, & \text{if } r_A \leq d_1, 22.5 < h_A \leq 100 \\ 1, & \text{if } 100 < h_A \leq 300, \end{cases} \quad (22)$$

where $d_1 = \max(294.05 \log_{10}(h_A) - 432.94, 18)$ and $p_1 = 233.98 \log_{10}(h_A) - 0.95$. The probability of LoS at $h_A = 25$ m is illustrated in Fig. 12. Compared with ITU LoS probability for the same height from Fig. 5(a), we can see that the LoS probability is very favorable even at low height of AUE.

The trajectory model for this scenario is defined as follows. The AUE starts its trajectory at a random initial location at the cell edge. Then, it moves at a randomly selected orientation in a straight line until it reaches the cell edge. Once it reaches the cell border, it picks another random orientation and moves in a straight line, and this process is continued until the AUE reaches its final trajectory point. An example realization, used for the purposed of generating results, is shown in Fig. 11. We consider AUE moves along multiple chords in the cellular cell, where A, B, C, D, E, and F correspond to the points at the cell edge where AUE changes the orientation of the trajectory. We consider that AUE transmits 10 times along its trajectory (see Fig. 11).

Fig. 13 presents the model validation results for the 3GPP probabilistic LoS and mobility model. We can see that simulation results match well with the analytical results. This confirms that our proposed NOMA model can be applied to any trajectory model. We can see that the trajectory point at $n = 7$, has the highest total rate coverage probability. This is because at this point the AUE has close proximity to the terrestrial BS, and this is consistent with the trends discussed in the previous trajectory model. Fig. 14 illustrates the minimum height of AUE that satisfies a target QoS requirement of 90%. Note that, at $\theta_A = 30$ dB, trajectory points $n = 4$ and $n = 10$, fail to meet this QoS requirement within the given height range. This is due to the fact that these transmission points are located very close to the cell edge. We can see that for $\theta_A = 20$ and 30 dB, the minimum height required to maintain a QoS of 90% increases and decreases at various points in the trajectory. This trend is different from the Archimedes' spiral trajectory where the minimum height increases as the AUE moves from the center to the cell edge. This highlights the importance of considering the specific UAV mobility in the modeling and design of UAV communication systems.

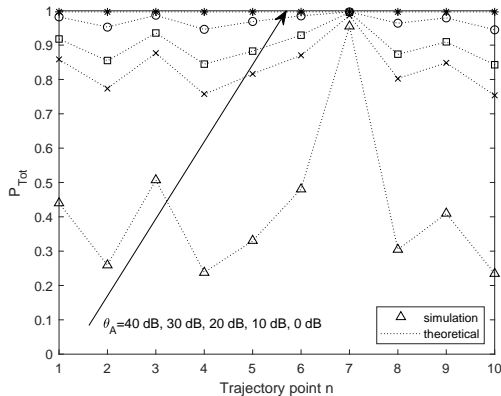


Fig. 13. P_{Tot} for 3GPP-inspired trajectory model and probabilistic LoS model. The simulation values and the theoretical values are represented by bullets and dotted lines, respectively.

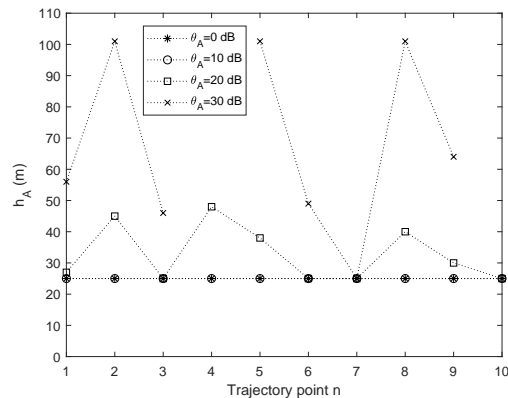


Fig. 14. The minimum height of AUE to achieve a target QoS of 90% at each trajectory point in the urban environment for 3GPP-inspired trajectory model and probabilistic LoS model.

VI. CONCLUSION

In this paper, we considered the coexistence of an AUE with a paired TUEs in a cellular network. We assumed that the AUE flies in a given trajectory path and transmits to the BS periodically. To facilitate the concurrent uplink transmissions of the AUE and the TUE, we used an aerial-terrestrial NOMA scheme with SIC at the BS. We formulated an analytical framework that evaluates the rate coverage probability of each user and the system, at each transmission point on the trajectory. The numerical results showed that, for the spiral trajectory, the rate coverage probabilities decrease as the target data rate of the AUE increases and the AUE moves away from the BS. We also found the minimum height of AUE at each trajectory point in order to meet a QoS of 90% for different built-up environments. In the spiral trajectory, it was observed that the minimum height increases as the environmental parameters become more severe and when AUE moves towards the cell edge. For the trajectory model adopted from the 3GPP recommendations, it was observed that the minimum height increases and decreases depending on the distance of AUE from the BS.

APPENDIX A

PROOF OF LEMMA 1

The horizontal distance r_T between the active TUE and BS at the time of transmission follows an uniform distribution due to the fact that x_T and y_T are uniformly distributed in the circular

cell. Thus, the pdf of r_T is $f_{r_T}(r) = \frac{2r}{R^2}$. The 3D distance d_T between the BS and TUE is given by $d_T = \sqrt{h_{BS}^2 + R^2}$. Therefore, the pdf of d_T is derived as

$$f_{d_T}(z) = \frac{dr}{dz} f_{r_T}(r) = \frac{d(\sqrt{z^2 - h_{BS}^2})}{dz} f_{r_T}(\sqrt{z^2 - h_{BS}^2}) = \frac{z}{\sqrt{z^2 - h_{BS}^2}} \frac{2\sqrt{z^2 - h_{BS}^2}}{R^2} = \frac{2z}{R^2}. \quad (23)$$

APPENDIX B

PROOFS OF LEMMAS 2 AND 3

In this appendix, we provide proofs of Lemmas 2 and 3.

A. Proof of Lemma 2

The CDF of ψ_T can be written as

$$\begin{aligned} F_{\psi_T}(x) &= \mathbb{P}_{d_T, H_T} (P_T d_T^{-\alpha_T} H_T G_T < x) \\ &= \mathbb{E}_{d_T} \left[\mathbb{P} \left(H_T < \frac{x}{P_T d_T^{-\alpha_T} G_T} \right) \right] \\ &= \mathbb{E}_{d_T} \left[1 - \exp \left(-\frac{x}{P_T d_T^{-\alpha_T} G_T} \right) \right] \end{aligned} \quad (24a)$$

$$= 1 - \int_{h_{BS}}^{\sqrt{h_{BS}^2 + R^2}} \exp \left(\frac{-x}{\rho_T z^{\alpha_T} z^{-\alpha_T} G_T} \right) \left(\frac{2z}{R^2} \right) dz \quad (24b)$$

$$= 1 - \exp \left(\frac{-x}{\rho_T G_T} \right), \quad (24c)$$

where (24a) comes from the fact that H_T follows an exponential distribution. (24b) is the expectation with respect to d_T , where $P_T = \rho_T z^{-\alpha_T}$ and $f_{d_T}(z) = \frac{2z}{R^2}$. Taking the derivative of $F_{\psi_T}(x)$ with respect to x we obtain its PDF.

B. Proof of Lemma 3

The CDF of ψ_A can be expressed as

$$\begin{aligned} F_{\psi_A}(x) &= \mathbb{P}_{H_A, d_A} (P_A \zeta_A H_A G_A < x) \\ &= \mathbb{E}_{d_A} \left[\mathbb{P} \left(H_A < \frac{x}{P_A \zeta_A G_A} \right) \right] \\ &= \mathbb{E}_{d_A} \left[1 - \mathbb{P}_{\text{LoS}} \sum_{i=0}^{m_L-1} \left(\frac{m_L x}{P_A \eta_L d_A^{-\alpha_L} G_A} \right)^i \frac{1}{i!} \exp \left(\frac{-m_L x}{P_A \eta_L d_A^{-\alpha_L} G_A} \right) \right. \\ &\quad \left. - (1 - \mathbb{P}_{\text{LoS}}) \sum_{j=0}^{m_N-1} \left(\frac{m_N x}{P_A \eta_N d_A^{-\alpha_N} G_A} \right)^j \frac{1}{j!} \exp \left(\frac{-m_N x}{P_A \eta_N d_A^{-\alpha_N} G_A} \right) \right] \end{aligned} \quad (25a)$$

$$= 1 - \mathbb{P}_{\text{LoS}} \sum_{i=0}^{m_L-1} \frac{(\beta_L x)^i}{i!} \exp(-\beta_L x) - (1 - \mathbb{P}_{\text{LoS}}) \sum_{j=0}^{m_N-1} \frac{(\beta_N x)^j}{j!} \exp(-\beta_N x), \quad (25b)$$

where (25a) comes from the fact that H_A follows a Gamma distribution with parameters m_L and m_N for LoS and NLoS A2C channel link respectively. Also, note that the expectation in (25a) is a constant due to the fact that d_A is a deterministic variable. $f_{\psi_A}(x)$ can be derived by taking the derivative of $F_{\psi_A}(x)$ with respect to x .

APPENDIX C

PROOFS OF PROPOSITIONS 1 AND 2

In this appendix, we provide the proofs of Propositions 1 and 2.

A. Proof of Proposition 1

The rate coverage probability P_1 can be expressed as

$$P_1 = \mathbb{P}_{\psi_A, \psi_T} \left(\frac{\psi_T}{\sigma^2} \geq \theta_T, \frac{\psi_A}{\psi_T + \sigma^2} \geq \theta_A \right) \\ = \mathbb{E}_{\psi_T} \left[\mathbb{P}_{\psi_A} (t \geq \theta_T \sigma^2, \psi_A \geq \theta_A (t + \sigma^2)) \right] \quad (26a)$$

$$= \int_{\theta_T \sigma^2}^{\infty} \mathbb{P}_{\psi_A} (\psi_A \geq \theta_A (t + \sigma^2)) f_{\psi_T}(t) dt \quad (26b)$$

$$= \int_{\theta_T \sigma^2}^{\infty} \mathbb{P} \left(H_A \geq \frac{\theta_A (t + \sigma^2)}{P_A \zeta_A G_A} \right) f_{\psi_T}(t) dt$$

$$= \int_{\theta_T \sigma^2}^{\infty} \left(\mathbb{P}_{\text{LoS}} \sum_{i=0}^{m_L-1} \frac{(\beta_L \theta_A)^i}{i!} (t + \sigma^2)^i \exp(-\beta_L \theta_A (t + \sigma^2)) \right. \\ \left. + (1 - \mathbb{P}_{\text{LoS}}) \sum_{j=0}^{m_N-1} \frac{(\beta_N \theta_A)^j}{j!} (t + \sigma^2)^j \exp(-\beta_N \theta_A (t + \sigma^2)) \right) f_{\psi_T}(t) dt \quad (26c)$$

$$= \mathbb{P}_{\text{LoS}} \sum_{i=0}^{m_L-1} \frac{(\beta_L \theta_A)^i}{i!} \frac{1}{\rho_T G_T} \exp\left(\frac{\sigma^2}{\rho_T G_T}\right) \left(\beta_L \theta_A + \frac{1}{\rho_T G_T}\right)^{-i-1} \\ \times \Gamma\left(i+1, \frac{(1+\theta_T)(1+\beta_L \theta_A \rho_T G_T) \sigma^2}{\rho_T G_T}\right) + (1 - \mathbb{P}_{\text{LoS}}) \sum_{j=0}^{m_N-1} \frac{(\beta_N \theta_A)^j}{j!} \frac{1}{\rho_T G_T} \exp\left(\frac{\sigma^2}{\rho_T G_T}\right) \\ \times \left(\beta_N \theta_A + \frac{1}{\rho_T G_T}\right)^{-j-1} \Gamma\left(j+1, \frac{(1+\theta_T)(1+\beta_N \theta_A \rho_T G_T) \sigma^2}{\rho_T G_T}\right). \quad (26d)$$

In (26a) we consider that t denotes a random variable with distribution $f_{\psi_T}(t)$ and it is a constant with respect to the random variable ψ_A . Expectation with respect to t , and lower and upper boundaries of t are applied in (26b). (26c) comes from the fact that the fading of AUE has a

Gamma distribution and, (26d) is obtained by integrating (26c) with respect to t . Finally, (10) can be derived by substituting $\mu = \rho_T G_T$ into (26d).

B. Proof of Proposition 2

The rate coverage probability P_2 can be expressed as

$$\begin{aligned} P_2 &= \mathbb{P}_{\psi_A, \psi_T} \left(\frac{\psi_T}{\sigma^2} < \theta_T, \frac{\psi_A}{\psi_T + \sigma^2} \geq \theta_A \right) \\ &= \mathbb{E}_{\psi_T} \left[\mathbb{P}_{\psi_A} (t < \theta_T \sigma^2, \psi_A \geq \theta_A (t + \sigma^2)) \right] \\ &= \int_0^{\theta_T \sigma^2} \mathbb{P}_{\psi_A} (\psi_A \geq \theta_A (t + \sigma^2)) f_{\psi_T}(t) dt \\ &= \int_0^{\theta_T \sigma^2} \left(\mathbb{P}_{\text{LoS}} \sum_{i=0}^{m_L-1} \frac{(\beta_L \theta_A)^i}{i!} (t + \sigma^2)^i \exp(-\beta_L \theta_A (t + \sigma^2)) \right. \end{aligned} \quad (27a)$$

$$\left. + (1 - \mathbb{P}_{\text{LoS}}) \sum_{j=0}^{m_N-1} \frac{(\beta_N \theta_A)^j}{j!} (t + \sigma^2)^j \exp(-\beta_N \theta_A (t + \sigma^2)) \right) f_{\psi_T}(t) dt, \quad (27b)$$

where the derivation of $P_{\psi_A}(\theta_A(t + \sigma^2))$ in (27a) is same as that in (26). (11) can be obtained by integrating (27b) with respect to t .

REFERENCES

- [1] N. Senadhira, S. Durrani, X. Zhou, N. Yang, and M. Ding, "Impact of UAV trajectory on NOMA-assisted cellular-connected UAV networks," in *Proc. IEEE ICC (submitted)*, Oct. 2019.
- [2] G. Geraci, A. Garcia-Rodriguez, and X. Lin, "Preparing the ground for drone communications," Jun. 2019. [Online]. Available: <https://www.comsoc.org/publications/ctn/preparing-ground-drone-communications>
- [3] Y. Zeng, Q. Wu, and R. Zhang, "Accessing From The Sky: A Tutorial on UAV Communications for 5G and Beyond," *arXiv:1903.05289*, Mar. 2019.
- [4] M. Mozaffari, W. Saad, M. Bennis, Y. Nam, and M. Debbah, "A tutorial on UAVs for wireless networks: Applications, challenges, and open problems," *IEEE Commun. Surveys Tuts.*, vol. 21, no. 3, pp. 2334–2360, Mar. 2019.
- [5] X. Lin, V. Yajnanarayana, S. D. Muruganathan, S. Gao, H. Asplund, H. Maattanen, M. Bergstrom, S. Euler, and Y. . E. Wang, "The sky is not the limit: LTE for unmanned aerial vehicles," *IEEE Commun. Mag.*, vol. 56, no. 4, pp. 204–210, Apr. 2018.
- [6] A. Fotouhi, H. Qiang, M. Ding, M. Hassan, L. G. Giordano, A. Garcia-Rodriguez, and J. Yuan, "Survey on UAV cellular communications: Practical aspects, standardization advancements, regulation, and security challenges," *IEEE Commun. Surveys Tuts.*, pp. 1–1, Mar. 2019.
- [7] Y. Zeng, J. Lyu, and R. Zhang, "Cellular-connected UAV: potential, challenges, and promising technologies," *IEEE Wirel. Commun.*, vol. 26, no. 1, pp. 120–127, Feb. 2019.
- [8] Nokia, "F-Cell technology from nokia bell labs revolutionizes small cell deployment by cutting wires, costs and time," Oct. 2016. [Online]. Available: <https://www.nokia.com/about-us/news/releases/2016/10/03/f-cell-technology-from-nokia-bell-labs-revolutionizes-small-cell-deployment-by-cutting-wires-costs-and-time/>

- [9] Huawei, "Digital sky initiative," Nov. 2017. [Online]. Available: <https://www.huawei.com/en/industry-insights/outlook/mobile-broadband/xlabs/industry-views/digital-sky-initiative>
- [10] R. Amer, W. Saad, H. ElSawy, M. Butt, and N. Marchetti, "Caching to the sky: Performance analysis of cache-assisted CoMP for cellular-connected UAVs," *arXiv:1811.11098*, Nov. 2018.
- [11] L. Dai, B. Wang, Z. Ding, Z. Wang, S. Chen, and L. Hanzo, "A survey of non-orthogonal multiple access for 5G," *IEEE Commun. Surveys Tuts.*, vol. 20, no. 3, pp. 2294–2323, May 2018.
- [12] M. Liaqat, K. A. Noordin, T. A. Latef, and K. Dimiyati, "Power-domain non orthogonal multiple access (PD-NOMA) in cooperative networks: an overview," *Wirel. Netw.*, pp. 1–23, Jul. 2018.
- [13] X. Su, A. Castiglione, C. Esposito, and C. Choi, "Power domain NOMA to support group communication in public safety networks," *Futur. Gener. Comp. Sy.*, vol. 84, pp. 228–238, Jul. 2018.
- [14] Y. Liu, Z. Qin, Y. Cai, Y. Gao, G. Y. Li, and A. Nallanathan, "UAV communications based on non-orthogonal multiple access," *IEEE Wirel. Commun.*, vol. 26, no. 1, pp. 52–57, Feb. 2019.
- [15] N. Rupasinghe, Y. Yapc, I. Gven, and Y. Kakishima, "Non-orthogonal multiple access for mmwave drone networks with limited feedback," *IEEE Trans. Commun.*, vol. 67, no. 1, pp. 762–777, Jan. 2019.
- [16] R. Duan, J. Wang, C. Jiang, H. Yao, Y. Ren, and Y. Qian, "Resource allocation for Multi-UAV aided IoT NOMA uplink transmission systems," *IEEE Internet Things J.*, Aug. 2019.
- [17] N. Zhao, X. Pang, Z. Li, Y. Chen, F. Li, Z. Ding, and M. Alouini, "Joint trajectory and precoding optimization for UAV-Assisted NOMA networks," *IEEE Trans. Commun.*, vol. 67, no. 5, pp. 3723–3735, May 2019.
- [18] J. Sun, Z. Wang, and Q. Huang, "Cyclical NOMA based UAV-enabled wireless network," *IEEE Access*, vol. 7, pp. 4248–4259, Dec. 2019.
- [19] L. Liu, S. Zhang, and R. Zhang, "Exploiting NOMA for multi-beam UAV communication in cellular uplink," in *Proc. IEEE ICC*, May 2019, pp. 1–6.
- [20] W. Mei and R. Zhang, "Uplink cooperative NOMA for cellular-connected UAV," *IEEE J. Sel. Topics Signal Process.*, vol. 13, no. 3, pp. 644–656, Jun. 2019.
- [21] A. Rahmati, Y. Yapici, N. Rupasinghe, I. Guvenc, H. Dai, and A. Bhuyan, "Energy efficiency of RSMA and NOMA in cellular-connected mmWave UAV networks," in *Proc. IEEE ICC Workshops*, May 2019.
- [22] J. Lyu, Y. Zeng, R. Zhang, and T. J. Lim, "Placement optimization of UAV-Mounted mobile base stations," *IEEE Commun. Lett.*, vol. 21, no. 3, pp. 604–607, Mar. 2017.
- [23] M. Alzenad, A. El-Keyi, and H. Yanikomeroglu, "3-D placement of an unmanned aerial vehicle base station for maximum coverage of users with different QoS requirements," *IEEE Wireless Commun. Lett.*, vol. 7, no. 1, pp. 38–41, Feb. 2018.
- [24] M. M. U. Chowdhury, E. Bulut, and I. Guvenc, "Trajectory optimization in UAV-assisted cellular networks under mission duration constraint," in *Proc. IEEE RWS*, Jan. 2019, pp. 1–4.
- [25] Y. Huang, J. Xu, L. Qiu, and R. Zhang, "Cognitive UAV communication via joint trajectory and power control," in *Proc. IEEE SPAWC*, Jun. 2018, pp. 1–5.
- [26] D. Yang, Q. Wu, Y. Zeng, and R. Zhang, "Energy tradeoff in ground-to-UAV communication via trajectory design," *IEEE Trans. Veh. Technol.*, vol. 67, no. 7, pp. 6721–6726, Jul. 2018.
- [27] C. Zhang and W. Zhang, "Spectrum sharing for drone networks," *IEEE J. Sel. Areas Commun.*, vol. 35, no. 1, pp. 136–144, Jan. 2017.
- [28] V. V. Chetlur and H. S. Dhillon, "Downlink coverage analysis for a finite 3-D wireless network of unmanned aerial vehicles," *IEEE Trans. Commun.*, vol. 65, no. 10, pp. 4543–4558, Oct. 2017.
- [29] A. Al-Hourani, S. Kandeepan, and S. Lardner, "Optimal LAP altitude for maximum coverage," *IEEE Wireless Commun. Lett.*, vol. 3, no. 6, pp. 569–572, Dec. 2014.

- [30] Y. Zhang, P. Ren, L. Sun, Q. Du, and Y. Wang, "Antenna tilt assignment for three-dimensional beamforming in multiuser systems," in *Proc. IEEE GLOBECOM*, Dec. 2015, pp. 1–6.
- [31] D. Lopez-Prez, M. Ding, H. Li, L. G. Giordano, G. Geraci, A. Garcia-Rodriguez, Z. Lin, and M. Hassan, "On the downlink performance of UAV communications in dense cellular networks," in *Proc. IEEE GLOBECOM*, Dec. 2018.
- [32] S. Enayati, H. Saeedi, H. Pishro-Nik, and H. Yanikomeroglu, "Moving aerial base station networks: A stochastic geometry analysis and design perspective," *IEEE Trans. Wireless Commun.*, vol. 18, no. 6, pp. 2977–2988, Jun. 2019.
- [33] P. K. Sharma and D. I. Kim, "Coverage probability of 3-D mobile UAV networks," *IEEE Wireless Commun. Lett.*, vol. 8, no. 1, pp. 97–100, Feb. 2019.
- [34] M. Banagar and H. S. Dhillon, "3GPP-inspired stochastic geometry-based mobility model for a drone cellular network," *arXiv:1905.00972*, May 2019.
- [35] A. A. Khuwaja, Y. Chen, N. Zhao, M. Alouini, and P. Dobbins, "A survey of channel modeling for UAV communications," *IEEE Commun. Surveys Tuts.*, vol. 20, no. 4, pp. 2804–2821, Jul. 2018.
- [36] X. Zhou, S. Durrani, J. Guo, and H. Yanikomeroglu, "Underlay drone cell for temporary events: Impact of drone height and aerial channel environments," *IEEE Internet Things J.*, vol. 6, no. 2, pp. 1704–1718, Apr. 2019.
- [37] H. ElSawy and E. Hossain, "On stochastic geometry modeling of cellular uplink transmission with truncated channel inversion power control," *IEEE Trans. Wireless Commun.*, vol. 13, no. 8, pp. 4454–4469, Aug. 2014.
- [38] H. Tabassum, E. Hossain, and J. Hossain, "Modeling and analysis of uplink non-orthogonal multiple access in large-scale cellular networks using Poisson cluster processes," *IEEE Trans. Commun.*, vol. 65, no. 8, pp. 3555–3570, Aug. 2017.
- [39] M. Salehi, H. Tabassum, and E. Hossain, "Accuracy of distance-based ranking of users in the analysis of NOMA systems," *IEEE Trans. Communications*, vol. 67, no. 7, pp. 5069–5083, Oct. 2019.
- [40] J. Wang, B. Xia, K. Xiao, Y. Gao, and S. Ma, "Outage performance analysis for wireless non-orthogonal multiple access systems," *IEEE Access*, vol. 6, pp. 3611–3618, Jan. 2018.
- [41] H. Sun, B. Xie, R. Q. Hu, and G. Wu, "Non-orthogonal multiple access with SIC error propagation in downlink wireless MIMO networks," in *Proc. VTC-Fall*, Sep. 2016.
- [42] B. Xia, J. Wang, K. Xiao, Y. Gao, Y. Yao, and S. Ma, "Outage performance analysis for the advanced SIC receiver in wireless NOMA systems," *IEEE Trans. Veh. Technol.*, vol. 67, no. 7, pp. 6711–6715, Jul. 2018.
- [43] 3GPP, "3GPP TR 36.777: Study on enhanced LTE support for aerial vehicles (release 15)," 2017.
- [44] ITU, "Recommendation p.1410-5: Propagation data and prediction methods required for the design of terrestrial broadband radio access systems operating in a frequency range from 3 to 60 GHz," *Tech. Rep.*, Feb. 2012.
- [45] N. Cherif, M. Alzenad, H. Yanikomeroglu, and A. Yongacoglu, "Downlink Coverage and Rate Analysis of an Aerial User in Integrated Aerial and Terrestrial Networks," *arXiv:1905.11934*, May 2019.
- [46] J. Holis and P. Pechac, "Elevation dependent shadowing model for mobile communications via high altitude platforms in built-up areas," *IEEE Trans. Antennas Propag.*, vol. 56, no. 4, pp. 1078–1084, Apr. 2008.